UCLA
UCLA Previously Published Works

Title

Haptic artificial muscle skin for extended reality

Permalink

https://escholarship.org/uc/item/4n28h5rh

Journal

Science Advances, 10(43)

ISSN

2375-2548

Authors

Guo, Yuxuan

Luo, Yang

Plamthottam, Roshan

et al.

Publication Date

2024-10-25

DOI

10.1126/sciadv.adr1765

Peer reviewed

Haptic artificial muscle skin for extended reality

Yuxuan Guo[1]†, Yang Luo[1]†, Roshan Plamthottam[1]†, Siyou Pei[2], Chen Wei[3], Ziqing Han[1], Jiacheng Fan[1], Mason Possinger[1], Kede Liu[1], Yingke Zhu[1], Zhangqing Fei[1], Isabelle Winardi[1], Hyeonji Hong[1], Yang Zhang[2], Lihua Jin[3], Qibing Pei[1,3]*

Existing haptic actuators are often rigid and limited in their ability to replicate real-world tactile sensations. We present a wearable haptic artificial muscle skin (HAMS) based on fully soft, millimeter-scale, multilayer dielectric elastomer actuators (DEAs) capable of significant out-of-plane deformation, a capability that typically requires rigid or liquid biasing. The DEAs use a thickness-varying multilayer structure to achieve large out-of-plane displacement and force, maintaining comfort and wearability. Experimental results demonstrate that HAMS can produce complex tactile feedback with high perception accuracy. Moreover, we show that HAMS can be integrated into extended reality (XR) systems, enhancing immersion and offering potential applications in entertainment, education, and assistive technologies.

INTRODUCTION

Current extended reality (XR) technologies, such as virtual reality (VR) and augmented reality (AR) head mounted displays, primarily enhance human experiences through interactive visuals and sounds. The next frontier of XR, however, aims to redefine immersion by incorporating the sense of touch, which holds the potential to revolutionize various fields, including entertainment, communication, education, and healthcare (1). Central to next-generation XR are haptic actuators that are responsible for generating and transmitting tactile sensations from the virtual environment to the mechanoreceptors nestled within our skin's dermis (2). While traditional haptic actuators have been integrated into XR interfaces such as controllers (3), gloves (4), or shoes (5), their bulky form factors and restriction to specific body parts lack versatility, impede dexterity during XR interaction, and limit users' immersive experience.

Skin-integrated haptic interfaces, which resemble skin-like patches, present a promising alternative with flexible adaptation to various body parts, thereby reducing intrusiveness and enabling natural interaction with virtual environments (6–8). Existing skin-integrated haptics predominantly use piezoelectric actuators (9) or magnetic motors (10) to create artificial sensory feedback in the form of mechanical vibrations, known as vibrotactile feedback. Nonetheless, the inherent rigidity of these actuators hinders the wearability of the XR devices. Moreover, due to their low strokes, these devices often operate at frequencies more than 100 Hz to optimize human perception (6), which falls short in accurately replicating real-world experiences where sustained force and lower frequencies are needed. In addition, they offer limited spatial resolution, typically up to 10 mm (11), posing challenges in delivering complex haptic feedback to smaller, more sensitive body parts, such as the fingertips.

Soft transducers, such as magnetic-responsive soft actuators (12), shape memory polymer actuators (13), fluidic soft actuators (14), and dielectric elastomer actuators (DEAs) (15) are promising alternatives. DEAs are particularly appealing due to their fast response, broad

bandwidth, large strains, high energy densities, and silent operation comparable to natural muscles, earning them the moniker "artificial muscles" (16). A typical DEA uses a dielectric elastomer (DE) thin film with compliant electrodes coated on its opposing sides. It contracts in the thickness direction and expands in-plane when placed under a voltage bias (17). While in-plane actuation can stretch the skin to create tactile sensation (15), this mode of stimulus is only sensitive to Ruffini corpuscles, a mechanosensory organ with a relatively low density within the skin (18). On the other hand, skin indentation can optimally stimulate a broader range of mechanoreceptors, including Meissner corpuscles, Merkel cells, and Pacinian corpuscles, allowing the replication of more complex physical interactions such as light touch, low- and high-frequency vibrations, sustained pressure, and weight perception (19).

Therefore, to effectively impart realistic tactile sensations, DEAs must generate significant out-of-plane output to indent the skin. One way to achieve out-of-plane motions in DEAs is to create a pressure difference between the opposing surfaces of the DE film (20). This approach usually necessitates an external pressure source and bulky pneumatic components such as pumps, chamber, tubes, and/or valves, which also renders the device susceptible to air leakage. Another strategy involves the use of stiff materials, such as embossed plastics (21, 22) or rigid indenters (23, 24), beneath the DEAs to induce buckling actuation. These solutions often compromise wearability and comfort, especially after prolonged use, due to the introduction of rigid components and can also adversely affect the performance (e.g., strain and/or force output) of the actuator. Embedding fluidic channels within DEAs to induce anisotropic deformation has been explored as an alternative (25), allowing for the fabrication of stretchable and conformal haptic interfaces (26). However, the resulting actuators have a maximum force output of 40 mN, potentially inadequate for areas of skin without high perception sensitivity. In addition, the introduction of a liquid significantly complicates the fabrication process, further limiting its widespread implementation.

Here, we present a wearable haptic artificial muscle skin (HAMS) based on a millimeter-scale, multilayered DEA capable of producing significant out-of-plane deformation and indenting the skin for optimal haptic stimuli (Fig. 1A). The DEAs harnessed an electric field gradient mechanism within a thickness-varied multilayer DE (TVMDE) to achieve out-of-plane deformation without an external

¹Department of Materials Science and Engineering, University of California, Los Angeles, Los Angeles, CA 90095, USA. ²Department of Electrical and Computer Engineering, University of California, Los Angeles, Los Angeles, CA 90095, USA. ³Department of Mechanical and Aerospace Engineering, University of California, Los Angeles, Los Angeles, CA 90095, USA.
*Corresponding author. Email: qpei@seas.ucla.edu
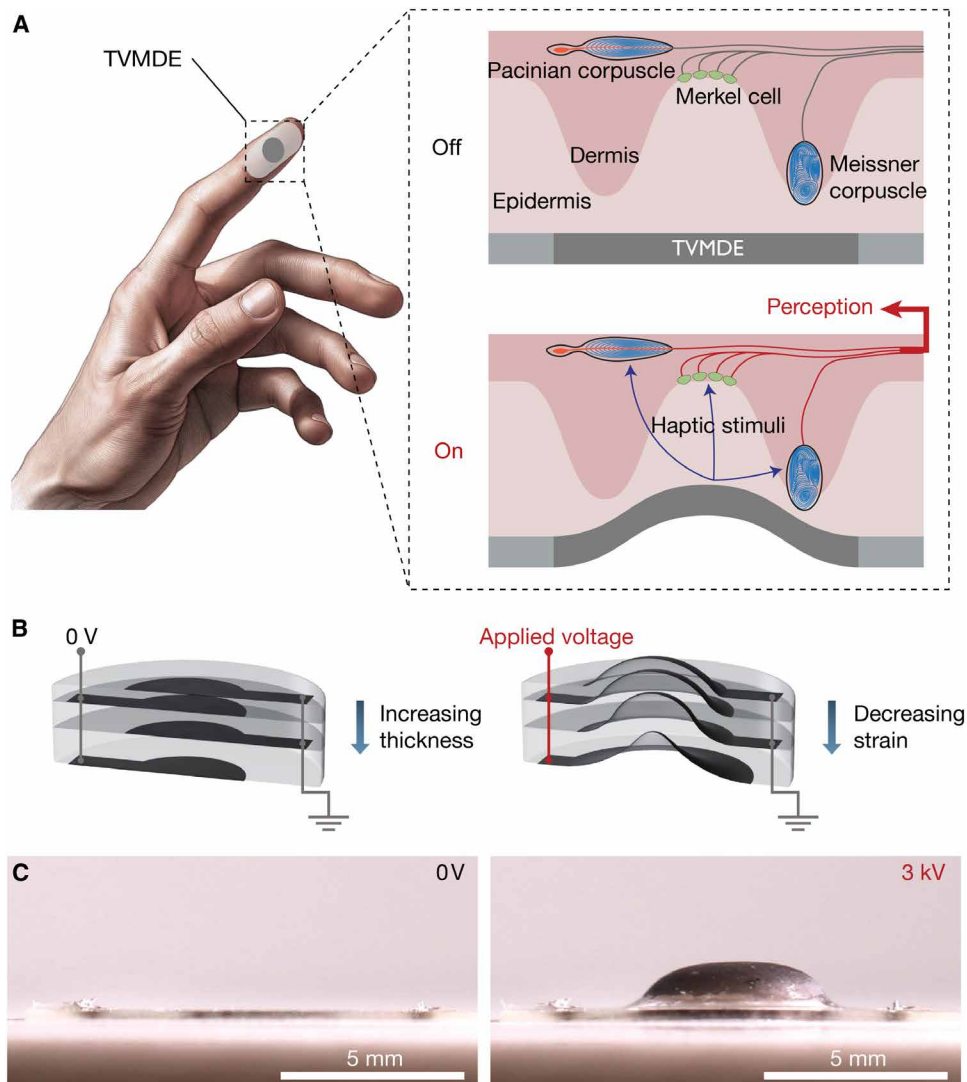†These authors contributed equally to this work.

Fig. 1. Working principle of the TVMDE. (**A**) Schematic illustration of how TVMDE, a skin-integrated soft actuator with out-of-plane actuation, enables effective tactile perception. When turned on, TVMDE deforms and indents the skin, stimulating multiple mechanosensory organs within the dermis, such as Meissner corpuscles, Merkel cells, and Pacinian corpuscles. These organs then send the haptic stimuli to the brain to complete the tactile perception process. (**B**) Schematic of a TVMDE design consisting of three layers of DE with gradually decreasing thicknesses. At a given voltage, thinner layers experience higher electric fields, resulting in a gradient actuation strain that ultimately leads to out-of-plane actuation. (**C**) Side-view images of a 10-layer TVMDE at rest (left) and during actuation at 3 kV (right).

pressure bias or any inactive, rigid components. This enabled HAMS to maintain a fully soft structure that conforms to a user's skin with optimal wearability and comfort. When seamlessly applied onto the user's body and connected to a VR headset, HAMS delivered an immersive XR experience with extended sensations that closely mimicked the tactile feedback of real-world interactions.

RESULTS

The actuation principle can be described by Fig. 1B. In this example, the multilayer consists of three layers of DEs with thicknesses that change gradually. Under a dc voltage bias, thinner layers experience larger electric fields than thicker ones, causing them to exhibit larger actuation strains. The resulting disparity in actuation strains enables the actuator to buckle out of plane in the direction of the thinner layers and output a force having a strong vertical component.

To ensure robust actuation, especially when individual layers are under different strain, strong interlayer adhesion is crucial. We developed a process to fabricate the TVMDE based on our recently reported processable high-performance DE (PHDE) and the corresponding multilayering process (*27*), as illustrated in fig. S1. This method ensures sufficient interlayer adhesion to prevent delamination during actuation. We began by preparing 40-μm-thick cured PHDE films, each coated with ultrathin single-walled carbon nanotubes (SWNTs) acting as the compliant electrodes. The PHDE precursor was diluted in acetone and sprayed in various amounts onto the SWNT-coated PHDE films to form PHDE precursor layers of various thicknesses (see detailed concentrations and quantities of

precursors sprayed in table S1). The modified PHDE films are then stacked to form the TVMDE, with each precursor layer being cured immediately after the addition of each new PHDE layer. The cured precursor layer not only acts as a binder to significantly enhance the interlayer adhesion, as evidenced by a swelling test (fig. S2), but also varies the total thickness of each PHDE layer in a scalable, controllable manner.

For practical implementations that require large force output, TVMDE configurations may extend beyond three layers. Our scalable process enabled large-area fabrication and customization in dimensions, array sizes, and layer counts for TVMDE (fig. S3 and see Materials and Methods for detailed fabrication process of TVMDE). This work focused on a 10-layer TVMDE with the following thickness configuration: The initial six layers each having 40 μm, followed by two layers of 45 μm, and concluding with two layers at 50 μm. Cross-sectional imaging using a scanning electron microscope of an as-fabricated 10-layer TVMDE revealed the seamless integration of the precursor with the bulk layers, effectively modifying the layer thicknesses (fig. S4). Figure 1C and movie S1 showed the out-of-plane actuation of a 10-layer TVMDE with an active area (circular overlapping area of the SWNT electrodes) diameter of 4 mm. Finite element analysis (FEA) of this setup also validated the anticipated buckling behavior under a 3-kV voltage (fig. S5 and see Materials and Methods for detailed simulation setup).

Experimental measurements of the displacement and force output of the 10-layer TVMDEs were performed to test their effectiveness as haptic stimuli. The diameter of active area in the TVMDEs was varied from 3 to 7 mm. Displacement was assessed by placing each actuator beneath a laser displacement sensor while subjecting it to a 0.5-Hz square wave voltage for static actuation (fig. S6A). Because of the transparency of SWNTs, a small reflective paint was applied at the center of each actuator's top surface to facilitate accurate sensor readings. Force output was measured by placing the actuators on a z-axis linear stage and contacting them with a force sensor to obtain minimal readings, typically below 0.3 mN (fig. S6B). The stage was then lowered until the sensor displayed zero, indicating no preload. The stage was further lowered for 30 μm, allowing TVMDE to buckle toward the probe. This setup approximated TVMDE's operation on skin, which, with skin being soft and flexible, provided low resistance to actuation and allowed the actuator to buckle despite being in contact with it.

As depicted in Fig. 2 (A and B), TVMDEs with larger diameters exhibited greater displacement and force output, as expected, due to the larger actuator geometry and active mass. This finding was consistent with the modeling results as well (Fig. 2C and see fig. S7 for additional simulated data). The displacement to diameter ratio (DDR) and specific force output, however, indicated that smaller actuators provided more efficient output (Fig. 2D). Furthermore, larger actuators decreased the spatial resolution of HAMS, required significantly more materials for their fabrication, and were more likely to contain defects that cause inferior performance or even failure. Considering these factors and to maintain sufficient absolute haptic output, we selected 4-mm TVMDEs for the remainder of this study.

Figure S8 showed the DDR and force output per unit area of this TVMDE, which compare favorably to other buckling actuators reported in literature (15, 22–24, 26, 28–30). In addition, the thickness-gradient approach minimized stress concentrations on the elastomer films in both active and inactive states. The monolithic design allowed the TVMDE to have a prolonged lifetime and retain its performance more than 200,000 cycles at a high voltage (Fig. 2E). As shown in fig. S9A, the TVMDE produced stable displacement over extensive continuous cycling. Two instances of drop-and-recover in the displacement profile were self-clearing events due to the fault-tolerant properties of thin SWNT electrodes (31, 32). Furthermore, TVMDE actuators stored for 12 months in an ambient environment still operated with minimal degradation in performance (fig. S9B). TVMDEs also demonstrated resilience in humid environments, as evidenced by the negligible loss in displacement output after being immersed in water for over 48 hours (fig. S9C).

Figure 2F and figure S10A showed the dynamic response of TVMDEs. At 3.5 kV, the 4-mm TVMDE retained around 50% of its displacement and force output at 25 Hz. Figure S10B plotted the typical displacement output of a 4-mm TVMDE under a 3-kV, 0.1-Hz square wave input. The rise time to reach 90% of its final free displacement is around 190 ms. Figure S10 (C and D) showed the displacement and force output profiles during a 2-Hz square-wave actuation.

Through the versatile fabrication process, the TVMDE design can incorporate pixels to realize the HAMS device. This was achieved by sandwiching an array of the TVMDEs between a thin elastomeric layer coated with stretchable conductive traces and a skin adhesive that provided robust adhesion to the skin (Fig. 3A and see fig. S11 for assembly process schematics). The elastomer layer was a 40-μm PHDE film, and the conductive paths were stencil-printed stretchable silver conductors. Electrical connections were established by puncturing the electrode leads on each actuator to reveal the interlayer SWNTs and subsequently filling the punctures with a conductive epoxy. This created both parallel connections between active DE layers and vertical interconnect accesses (VIAs) to the conductive path (Fig. 3B). Figure S12 showed the array dimension and conductive path design of the HAMS for this study. A custom flexible flat cable (FFC) was fabricated to extend HAMS's connection pads and provide robust connection to the external circuit (fig. S13). The skin adhesive was a copolymer of octadecyl acrylate (OA) and tetradecyl acrylate (TA) in a chemically crosslinked elastomer network (33), with a low modulus of 5 kPa at normal skin temperature and a high modulus of 67 MPa below 32°C (fig. S14). This allowed HAMS to be easily attached by pressing it on the skin and nondestructively detached upon cooling (movie S2). The adhesive layer also acted as an insulation layer to prevent charge dissipating from the actuators to skin.

The as-fabricated HAMS was a 600-μm-thick elastomer patch that can adapt to multiple mechanical manipulations such as bending and stretching (fig. S15). Apart from the color variations in the conductive materials, HAMS appeared skin-like, conforming seamlessly to the skin (Fig. 3C). In addition, HAMS formed a strong bond with the skin and maintained its adhesion strength through long hours of continuous wear and during activities that involve significant deformation of the skin.

While HAMS having 10-layer, 4-mm-diameter TVMDEs were the focus of this study, note that HAMS can also be configured with different TVMDE dimension, number of stacked DE layers, and/or array sizes tailored for different parts of the body. For example, HAMS integrated with a 2-by-2 array of five-layer, 2.5-mm-diameter TVMDE can fit on the fingertip, which outputs a maximum force of more than 80 mN at 3.5 kV (fig. S16).

To replicate complex, real-life tactile experiences, HAMS requires precise, individual control over each actuator element within
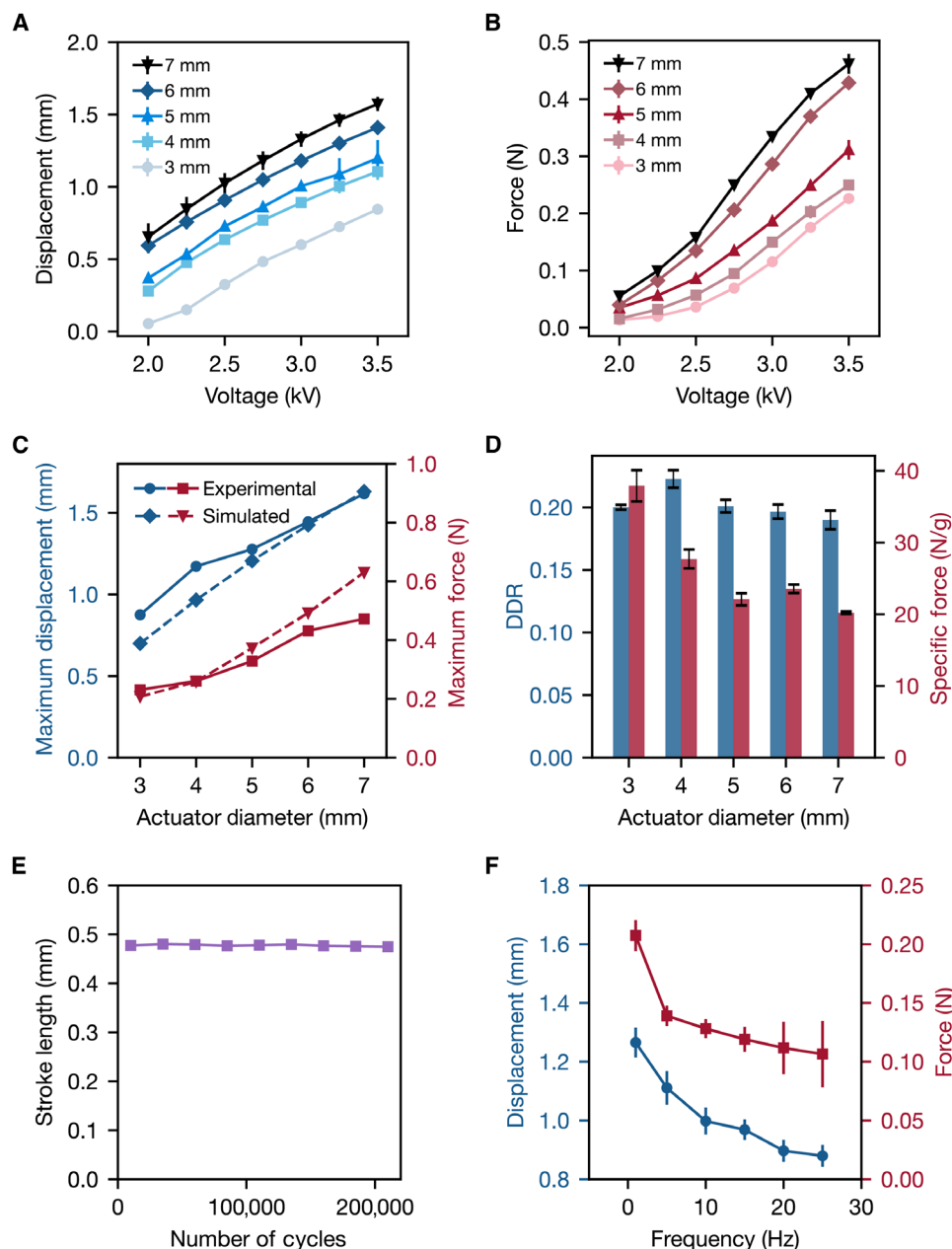
Fig. 2. Performance of the 10-layer TVMDE. Results with error bars indicate the average results ± SD for three samples. (**A**) Displacement versus voltage curve of samples with specified actuator diameter. (**B**) Force output versus voltage curve. (**C**) Maximum displacement and force output versus actuator diameter at 3.5 kV. Solid and dash lines represent experimental and simulated results, respectively. (**D**) Bar graph of the DDR and specific force output of the actuators versus diameter. (**E**) Measured stroke length (difference between maximum and minimum displacement in each cycle) of a 4-mm TVMDE actuator operated for over 200,000 cycles under a 20-Hz, 3.5-kV square-wave voltage. (**F**) Frequency response data of the 10-layer, 4-mm TVMDE actuators at 3.5 kV.

the array. In addition, producing meaningful deformation and force in DEAs necessitates applying an electric field exceeding 50 V/µm or several kilovolts across DE films that are merely tens of micrometers thick. While this poses safety considerations for a wearable device such as HAMS, the associated current and power consumption remain low due to the low capacitance of these actuators (*34*). To address these challenges, we used a battery-powered, high-voltage power supply (HVPS) with HV switching using multiple channels of optoelectronic half-bridge circuit (*35, 36*). More details about this

power supply can be found in fig. S17 and Materials and Methods. Our HVPS effectively actuated each element in HAMS at a current level less than 100 µA, with peak power consumption of less than 200 mW (figs. S18 to S19). This control scheme allowed for HAMS's safe operation on skin (movie S3) while providing individual addressing of the TVMDE in the array at a computer-programmable intensity and frequency (fig. S21). Figure 3D and movie S4 showed that a 3-by-3 HAMS can be programmed to display certain letters, either statically or dynamically.
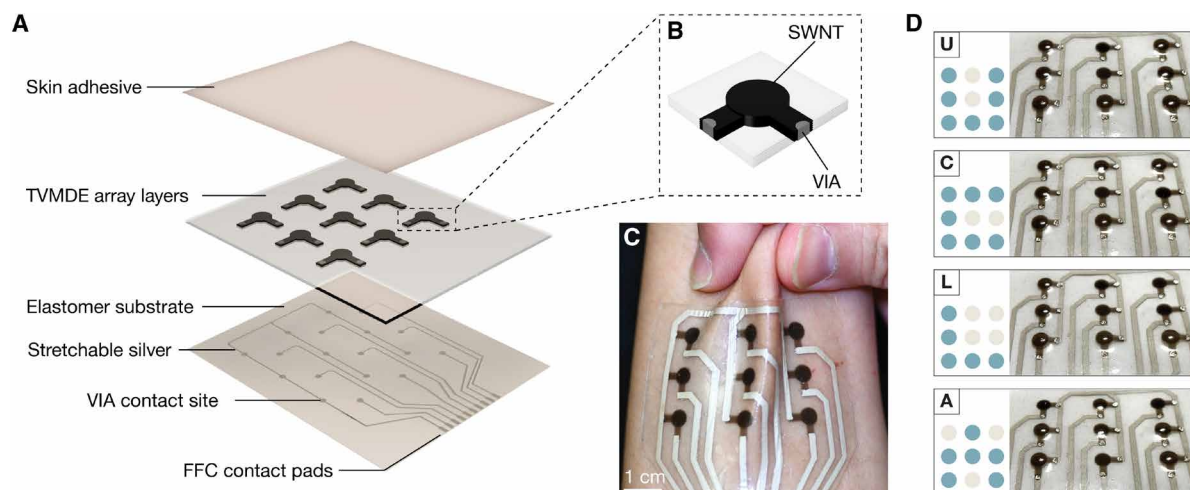
Fig. 3. Integration of HAMS. (A) Schematic illustration of the exploded view of a 3-by-3 HAMS. **(B)** Detailed schematic of an actuator element showing the VIA connection. **(C)** HAMS underwent severe deformation when attached to skin, showing robust adhesion and high stretchability. **(D)** Photographs of a HAMS programed to show patterns of "U," "C," "L," and "A." SWNT, single-walled carbon nanotube; FFC, flexible flat cable.

The threshold for static haptic perception, particularly on sensitive areas such as the fingertips and palm, is reported to be as low as 10 μm for displacement and 1.5 mN for force (*37*). However, the thresholds can vary considerably due to factors such as age, gender, and the characteristics of the stimulus, including its type and sequence. While a single TVMDE can produce static displacement and force significantly exceeding these thresholds, perception tests were performed to assess the effectiveness of HAMS when providing more dynamic haptic stimulations. We initially evaluated HAMS's ability to produce distinguishable haptic stimuli of varying intensity and frequency involving seven volunteers. A 3-by-3 HAMS was attached to the back of each participant's left hand. In the intensity differentiation test, participants were asked to identify haptic feedback at low, medium, and high intensities, which corresponded to activation voltages of 2, 2.25, and 2.5 kV, respectively. An "off" state was also included for control. The confusion matrix indicated high identification rates exceeding 82% for all intensity levels, with minimal confusion between adjacent intensities (Fig. 4A). The frequency test assessed each participant's perception of haptic feedback across five frequencies from 0.5 to 10 Hz. Participants demonstrated a consistent ability to perceive frequency changes, with accuracy rates surpassing 85% for all tested frequencies (Fig. 4B).

HAMS was then programmed to generate nine distinct patterns to evaluate its effectiveness in delivering more complex, spatiotemporal feedback. These patterns, depicted in fig. S22, include directional cues (right, left, down, and up) and more intricate movements such as radial ripples and rotational feedback that could simulate potential interactive events in the virtual environment. To ensure that differences in subject responses were due solely to the distinctiveness of the tactile patterns, all patterns were programmed with identical frequencies and comprised the same number of steps, eliminating variations in the signal's speed or rhythm. Almost all patterns showed correct identification rates of more than 80%, except the radial pattern (pattern number 7) at 71.4% (Fig. 4C). The slightly lower perception rate for the radial pattern may stem from

its less intuitive representation of motion. Overall, the identification rates for three perception tests were all agreeably high, averaging more than 90% (fig. S23). In each test, the identification rate between the off and "on" states of the HAMS was 100%, indicating that the participants can consistently detect when HAMS is activated, regardless of the type of actuation. This confirms that TVMDE actuators have sufficiently high stroke and force output such that their actuation is perceived through the adhesive layer. The generated tactile feedback is perceptible in varying intensities, frequencies, and sequences, enabling HAMS to replicate various dynamic and interactive experiences in the virtual environment.

Figure 5A illustrates the use of HAMS for immersive experiences within an XR system. During these tests, the user wore a commercial head-mounted display (HMD) and a 3-by-3 HAMS on the palm. The HMD, interfaced with the XR system, provided visual and auditory information of the virtual scenes created by Unity Engine on a personal computer (PC). The built-in hand tracking function in the HMD captured hand movements, while the scenes were scripted to detect collisions between the virtual hand and objects. Upon collision, the PC sent signals to the HVPS that generated specific haptic patterns on HAMS for realistic feedback. We demonstrated two dynamic scenarios: the perception of virtual rain (movie S5) and the manipulation of a virtual golf ball (movie S6). In the rain scene, users were placed in a digitally rendered rainy setting, where they could feel the raindrops on their hand (Fig. 5B). Leveraging HAMS's ability to modulate the intensity and frequency of the haptic feedback, the experience varied from the gentle and slow touch of light rain to the more pronounced and rapid sensation of a heavy downpour (Fig. 5C and movie S7). Users' interaction with the environment also affected the dynamic feedback; for instance, moving the hand under a parasol ceased the haptic sensation of rain. The golf simulation offered another layer of interaction, where users virtually grasped and manipulated a golf ball. As the ball rolled across the hand's surface, specific actuators on HAMS were activated, and a constant force was applied onto the hand to replicate the weight of the golf ball. The actuators mirrored the ball's movements and
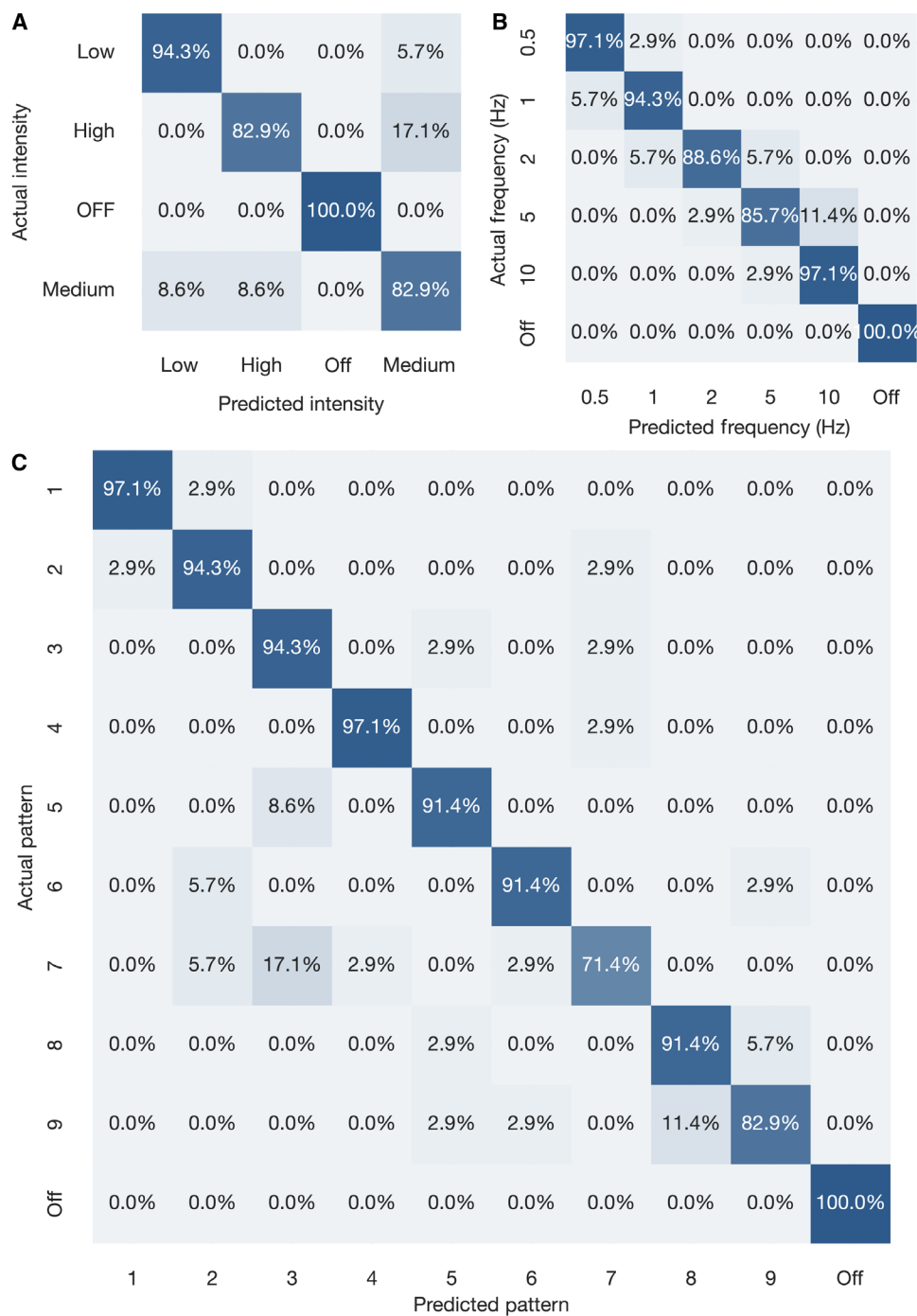
Fig. 4. Perception validation of HAMS. (**A**) Confusion matrix for the intensity test. Subjects were asked to identify the intensity of the actuation they received. (**B**) Confusion matrix for the frequency test. Subjects were asked to identify the frequency of the actuation they received. (**C**) Confusion matrix for the pattern test. Subjects were given actuation stimuli with 9 sets of patterns. Patterns 1 to 9 correspond to right, left, down, up, diagonal down, diagonal up, radial ripple, counter-clockwise rotation, and clockwise rotation, respectively.

changes in position until the ball rolled away (Fig. 5D and movie S8). Unlike traditional haptic interfaces that rely on high-frequency vibrotactile actuation, HAMS could generate a substantial vertical displacement over a long duration to apply a constant pressure on skin, effectively simulating the weight of the golf ball and enhancing the immersive experience.

DISCUSSION

We have successfully demonstrated HAMS, a fully soft, skin-integrated haptic interface, comprising millimeter-scale TVMDE actuators that achieve large out-of-plane actuation. A 4-mm TVMDE can generate a displacement of up to 1.36 mm and a force of up to 0.21 N while maintaining high performance with more than 200,000
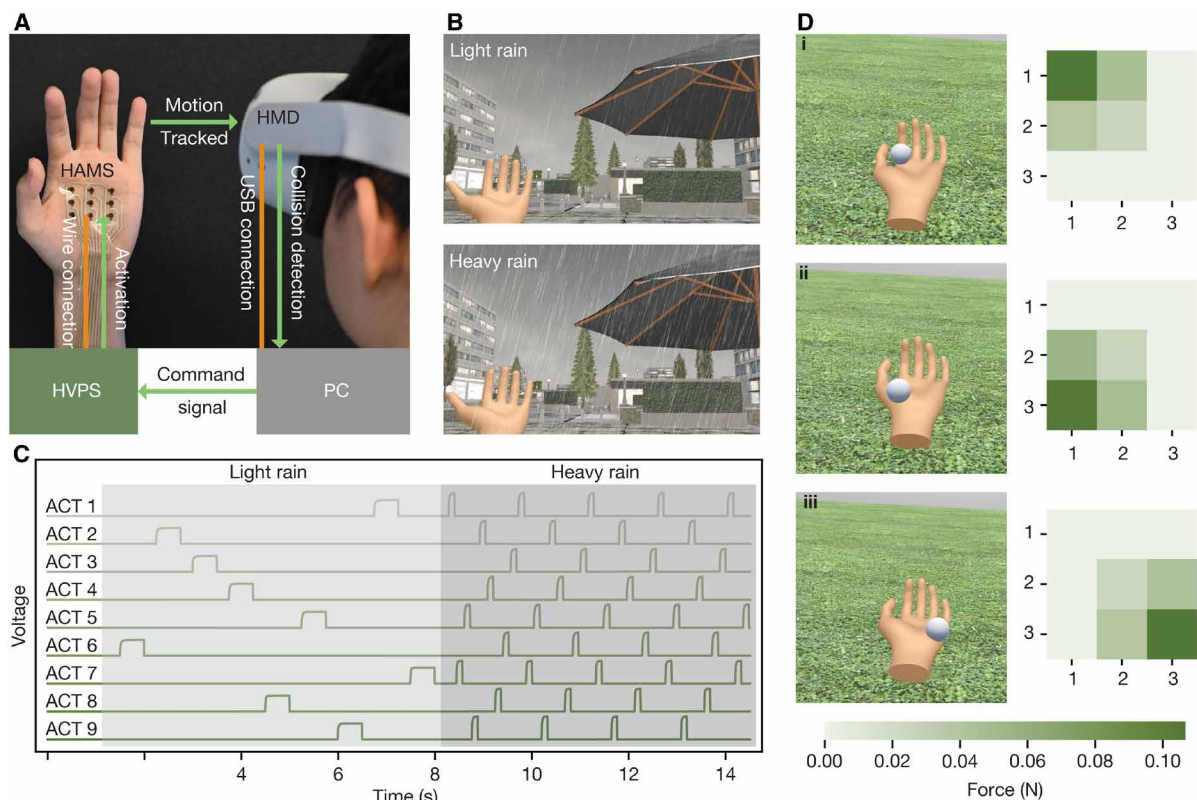
Fig. 5. XR demonstrations enabled by HAMS. (**A**) Photo of the user wearing HAMS and HMD for immersive XR experience. The HMD is connected to the PC via USB, and the HAMS is wired to the HVPS. (**B**) Experiencing rain. The top two images show screenshots of the rain scene during "light rain" and "heavy rain" conditions. Actuators received lower voltage inputs at lower frequencies to simulate light rain and higher voltage signals at higher frequencies to simulate heavy rain. (**C**) Real-time voltage across the nine actuators within HAMS when the weather went from light rain to heavy rain. (**D**) Demonstration of virtual object manipulation. The figure set depicts the incident when the user rolled a golf ball from (i) the top-left corner to (ii) bottom left corner to (iii) the bottom right corner in the palm. The left three figures show the virtual scene seen by the user, while the right figures display the heatmaps of the actuators' force output. Color bar is shown at the bottom.

cycles of continuous operation. With these soft and stable actuators and a skin adhesive, HAMS can be seamlessly and robustly attached to the skin, providing complex haptic feedback with more than 90% perception accuracy. The scalability and customizability of HAMS allow it to be applied to different skin surfaces and potentially cover the entire body. In addition, HAMS eliminates the rigid components typically found in wearable haptic devices and provides additional sensations such as sustained pressure on the skin, enhancing users' experience in XR environments. This work allows HAMS to potentially be used in applications such as XR entertainment and virtual training, as well as assistive technologies such as displaying Braille letters and indoor navigation for people with visual impairments.

MATERIALS AND METHODS
The following reagents were used in the synthesis of PHDE resin and adhesive polymer precursors: urethane diacrylate (UDA; catalog name: CN9021) and isobornyl acrylate (IBOA; catalog name: SR506A) were purchased from Sartomer; butyl acrylate (BA), acrylic acid (AA), propoxylate neopentyl glycol diacrylate (PNPDA), benzophenone (BP), OA, and 2,2-dimethoxy-2-phenylacetophenone (DMPA) were obtained from Sigma-Aldrich; TA was acquired from TCI America.

Preparation of the PHDE precursor resin
The preparation of the PHDE precursor was carried out by mixing the following reagents: UDA [70 (wt %)], PNPDA (10 wt %), IBOA (5 wt %), BA (13 wt %), AA (2.5 wt %), DMPA (1 wt %), and BP (0.5 wt %). The container holding the mixture was then immediately covered with aluminum foil, and the mixture was stirred overnight.

Fabrication of the TVMDE
The fabrication of TVMDE began with the preparation of single layer PHDE films. Making an N-layer TVMDE requires one PHDE film on a 170-μm-thick PET substrate and N-1 films on glass. The selected substrates provided different adhesion and stiffness to allow continuous addition of layers and avoid delamination during fabrication. Each film was made by blade-coating PHDE precursor solution onto glass or Polyethylene terephthalate (PET) substrates, followed by ultraviolet (UV) curing in nitrogen on a UV conveyor equipped with a Fusion 300 s–type "h" UV curing bulb (2.5 W/cm²) for two passes at a speed of 6 feet/min. Each film has a thickness of 40 μm, as controlled by the blade gap. All films were trimmed to ensure uniformity. SWNTs were then spray-coated onto glass/DE films with laser-cut masks to form patterned electrodes.

Next, each glass/DE film was sprayed with specific amount and concentration of the diluted precursor solution to adjust thickness

according to table S1. The precursor solution was diluted with acetone. Between layers that do not require thickness modification, i.e., the 40-μm layers, a thin layer of precursor solution was sprayed to act as a binder.

The stacking process is shown in fig. S1A. To initiate stacking, the PET/DE was aligned onto a glass/DE/SWNT/precursor, and the laminate was gently rolled to remove visible air bubble. The precursor layer was then UV cured in air on a UV conveyor equipped with Fusion 300 s–type "h" UV curing bulb (2.5 W/cm^2) for two passes at a speed of 6 feet/min. After UV curing, the glass was removed and the two-layer DE stack, which is now on PET, was aligned onto another glass/DE/SWNT/precursor to add the next DE layer. These processes were repeated until the desired layer number was reached.

Figure S1B shows layer cross sections during stacking of PET/DE and glass/DE/SWNT/precursor. Although the precursor layer was sprayed on the glass/DE, it added thickness to the DE layer on PET substrate.

Preparation of the TVMDE samples for testing

Individual TVMDEs were cut out and interlayer SWNT electrode leads were exposed. Parallel connection of the layers in a TVMDE were achieved by painting a silver epoxy (catalog name: 8331D, MG Chemicals) on the exposed electrode leads, as shown in fig. S1C. Electrical wires were then attached to the epoxy for connection to HV power. The silver epoxy was allowed to dry at room temperature for 1 hour.

Swelling test

The strong interlayer bonding of the TVMDE was assessed through a swelling test (fig. S2). A control sample consisting of 10 layers of 40-μm thick PHDE was laminated without any binder. Before testing, both the control and the TVMDE samples were well adhered and exhibited as a single film with an approximate area of 1 cm^2 each. After soaking in a tetrahydrofuran (THF) solution, the PHDE stack, which relied solely on van der Waals forces for bonding, delaminated completely within 1 min. In contrast, the TVMDE maintained strong interlayer adhesion and continued to perform as a robust, unified film even after 24 hours of soaking in THF.

FEA of the TVMDE

A general constitutive model of a DE

On the basis of previous studies on DEs (38–42), we used a general electromechanical constitutive model to capture the deformation of a DE under voltage. We considered a material particle labeled by a position vector $\mathbf{X}$ in the stress-free reference configuration Ω_0 ($\mathbf{X} \in \Omega_0$) that moves to the position $\mathbf{x}$ at time t in the current configuration Ω_c ($\mathbf{x} \in \Omega_c$). The deformation gradient was defined as $F_{iK} = \partial x_i(\mathbf{X}, t)/\partial X_K$. Voltage ϕ was applied across the opposite surfaces of the DE. We simplified the model by assuming that no extrinsic electric charge is present, and ϕ is constant. The electric field in the undeformed configuration was defined as $\overline{\mathbf{E}} = (\phi/H)\mathbf{N}$, where H is the thickness of the DE and $\mathbf{N}$ is the unit vector normal to the layer in the reference configuration from positive charge to negative charge.

We considered an ideal DE (38, 39), whose free energy is the sum of the elastic energy due to the network deformation and the free energy due to polarizing the dielectric. The free energy density of a DE in the reference configuration can be expressed as

$$f_r(\mathbf{F}, \overline{\mathbf{E}}) = f_{el}(\mathbf{F}) + f_{die}(\mathbf{F}, \overline{\mathbf{E}}) \tag{1}$$

The first term in Eq. 1

$$f_{el}(\mathbf{F}, \mathbf{d}) = -\frac{\mu}{2} J_m \cdot \ln\left(1 - \frac{I_1 - 3}{J_m}\right) - \mu \cdot \ln(J) + \left(\frac{K}{2} - \frac{\mu}{J_m}\right)(J - 1)^2 \tag{2}$$

describes the entropic elasticity of the elastomer network, known as the Gent model, where μ is the shear modulus, J_m is a fitting parameter, I_1 is the first invariant of $\mathbf{FF}^T$ defined as $I_1 := tr(\mathbf{FF}^T)$, K is the bulk modulus, and $J = \det(\mathbf{F})$. The second term in Eq. 1 is

$$f_{die}(\mathbf{F}, \overline{\mathbf{E}}) = \frac{\varepsilon J tr\left[\left(\mathbf{F}^{-T}\overline{\mathbf{E}}\right) \bigotimes \left(\mathbf{F}^{-T}\overline{\mathbf{E}}\right)\right]}{2} \tag{3}$$

where ε is the permittivity.

Considering the deformation of a DE as an equilibrium isothermal process, the thermodynamic condition requires the variation of the free energy of a DE over a small change should always equal the external work, $\int_{\Omega_0} \delta f_r dV = \delta W$. Here, we assumed that no body force or traction force was applied on the material so that $\delta W = 0$. Using the chain rule, we can get $\delta f_r = \partial f_r / \partial \mathbf{F} : \delta \mathbf{F} + \partial f_r / \partial \overline{\mathbf{E}} : \delta \overline{\mathbf{E}}$. As the applied voltage ϕ is constant, $\overline{\mathbf{E}}$ is constant and $\partial f_r / \partial \overline{\mathbf{E}} : \delta \overline{\mathbf{E}} = 0$. Then, we can derive the governing equation $div(\sigma) = 0$, where the Cauchy stress $\sigma = J^{-1} \partial f_r / \partial \mathbf{F} \mathbf{F}^T$ can be expressed as

$$\sigma = \frac{\mu J_m}{J_m - I_1 + 3} \frac{1}{J} \mathbf{FF}^T - \frac{\mu}{J} \mathbf{I} + 2(J - 1)\left(\frac{K}{2} - \frac{\mu}{J_m}\right)\mathbf{I} + \varepsilon \mathbf{E} \bigotimes \mathbf{E} - \frac{\varepsilon}{2} tr\left(\mathbf{E} \bigotimes \mathbf{E}\right)\mathbf{I} \tag{4}$$

where $\mathbf{E}$ represents the electric field in the current configuration, i.e., $\mathbf{E} = \mathbf{F}^{-T}\overline{\mathbf{E}}$.

Finite element simulation

We further implemented the DE model into the commercial finite element software, ABAQUS, via a user element subroutine, UMAT. The material parameters were fitted on the basis of the stress-strain data and the dielectric constant of PHDE (24)

$$\mu = 0.7099 \text{ MPa}, J_m = 4.3822, K/\mu = 1000,$$
$$\varepsilon = 4.7 \times 10^{-17} \text{ C}^2/(\text{N} \cdot \text{mm}^2) \tag{5}$$

where the bulk modulus K was set large enough to represent a nearly incompressible material. The model fitted well with the experimental stress-strain data as shown in fig. S5A.

To simulate the deformation of DE layers under a constant voltage across the thickness, we conducted static FEA in a model as shown in fig. S5B. Given the cylindrical shape of the actuator and the axisymmetric deformation, we used the four-node bilinear axisymmetric quadrilateral hybrid element. We simulated the cases with diameters of 3, 4, 5, 6, and 7 mm in the active region (where voltage was applied) and a width of 3 mm in the inactive region (no voltage applied). The external edge of the inactive part was fixed. Different DE layers were modeled on the basis of the geometry of the real actuators in the experiments. By varying the thickness of the DEs, different electrical field distributions were obtained,

$|\overline{\mathbf{E}}| = \phi/H$; thinner layers corresponded to higher electric fields. The contours in fig. S5 (B and C) show the electrical field and displacement distributions of a case with a diameter of 4 mm in the active region under 3.5 kV. We calculated the maximum displacements under voltage for different geometry and compared them with the experimental results (fig. S7).

To calculate the force output, we created a rigid section with an initial gap of 30 μm away from the top surface of the actuator, consistent with the experimental setup, to calculate the reaction force (fig. S5Bii). As the voltage increased, the constrained expansion of the DE induced compressive stress, which can lead to mechanical instability of the structure. To overcome the divergence of the simulations due to the instability, we conducted dynamic explicit analysis under quasi-static loading, which gave the same results as static analysis but can go beyond the instability. The predicted force output as a function of the voltage agreed well with the experimental measurements (fig. S7).

Displacement and force measurement on TVMDE
In the displacement tests, the laser displacement sensor (optoNCDT1420, Micro-Epsilon) was mounted around 15 mm above the actuators. A reflective dot with diameter of around 500 μm was carefully painted on the actuator using a blunt tip needle. Force output was measured by a force sensor (model M7-012, Mark-10 Corporation), which was mounted on a motorized stand (model ESM303, Mark-10 Corporation). An HV power amplifier (Trek 10/10B-HS, Advanced Energy) was used to generate square-wave voltage signal for the displacement and force measurement. A data acquisition board (model NI USB-6009, National Instruments) and a custom LabVIEW program were used to control the frequency and amplitude of the HV output.

Lifetime characterization of TVMDE
In the cyclic actuation test, a 4-mm, 10-layer TVMDE was positioned around 15 mm below the laser displacement sensor (optoNCDT1420, Micro-Epsilon). The actuator was then subject to a 20-Hz, 3.5-kV voltage until failure, and the displacement output was simultaneously recorded.

To test the resistance to humid environment, three 4-mm, 10-layer TVMDEs were immersed in deionized water for varying durations (0, 4, 12, 24, and 48 hours). After immersion, they were blow-dried before being actuated.

Fabrication of the skin adhesive
The precursor solution of the adhesive polymer was made by mixing UDA, OA, and TA in the ratio of 1:2:2, followed by adding 0.5 wt % of DMPA. The mixture was then sonicated for 30 min before injecting into a glass mold. The glass mold was made by gapping two pieces of water-repellent–coated glass slides with two 100-μm-thick polyester tape. The total tape thickness determined the final thickness of the adhesive. The precursor solution within the glass mold was then UV cured in air on a UV conveyor equipped with Fusion 300 s–type "h" UV curing bulb (2.5 W/cm^2) for one pass at a speed of 1 feet/min.

Fabrication of the stretchable electrode layer
The stretchable electrode layer consisted of a patterned stretchable silver conductor and a layer of PHDE as substrate. PHDE substrate was made by blade casting the precursor onto an 80-μm-thick release liner (MBK Tape Solution). The release liner had a silicone coating that allowed easy removal of the liner when integrating into HAMS, as explained in the next section. The precursor solution coated on the liner was then UV cured in nitrogen on a UV curing conveyor equipped with Fusion 300 s–type "h" UV curing bulb (2.5 W/cm^2) for two passes at a speed of 6 feet/min. The thickness of the final film on the liner had a thickness of 40 μm. Stretchable silver paste (catalog name: PE874, DuPont) was then printed on the PHDE through a laser-cut contact mask. The mask was then removed, and the silver/DE/liner was heated at 130°C for 15 min.

Assembly of a 3 × 3 HAMS
Circular through holes were created at the electrode leads on a 3 × 3 TVMDE array using a hollow metal punch with an inner diameter of 0.8 mm (fig. S11A). Then, the array was laminated onto the silver/DE/liner by aligning the holes with the VIA contact sites (fig. S11B). The punctures were then filled with the silver epoxy to form VIAs. The array/silver/DE/liner was then put on a hotplate at 35°C, and the skin adhesive was laminated on top. Last, the bottom release liner was removed.

Fabrication of the custom-made FFC and HAMS's connection strategy
An acrylic adhesive film (catalog name: F9469PC, 3M) with a thickness of 58 μm was first cut out with the liner attached. Next, a layer of stretchable silver conductor was printed on the adhesive through a laser-cut mask. After removing the mask, the silver/adhesive/liner was heated at 130°C for 15 min. A row of male pin header connectors with a pitch of 2.54 mm was aligned with the silver paths on one end of the FFC. Electrical connection between the pins and the silver paths was secured by applying the silver epoxy. A nonconducting epoxy adhesive (5 Minute Epoxy, Devcon) was applied at the contact points to provide electrical insulation and structural support. Then, the FFC can be connected to the control circuit through the pins.

The other side of the FFC was connected to the exposed FFC contact pads on HAMS. A thin layer of silver epoxy was applied in between to remove air gaps and to prevent high-voltage arcing. The exposed silver paths were covered by blade coating with the PHDE resin, followed by UV curing. Last, the liner for the adhesive layer was removed.

The HVPS
The block diagram of the HVPS used in this study was shown in fig. S17. This HVPS used a dc/dc converter (Model A05P-5, XP Power) to transform the 3.7-V dc input into 4 kV, which was then directed to nine pairs of commercial miniature HV optocouplers (model OPTO-150, HVM Technology) for switching. Each pair formed a half-bridge circuit responsible for the charging and discharging of individual actuators. A microcontroller (Teensy 4.1) applied a digital pulse width–modulated (PWM) signal to the light-emitting diode in each optocoupler. By adjusting the duty cycle of the PWM signals, we can regulate each channel's output voltage, thereby varying the intensity of the haptic feedback produced. The output frequency was tuned by programming the on and off time of the optocouplers.

Electrical characterization of the HVPS and TVMDE actuators
The voltage output of the HVPS was recorded using high-resolution Universal Serial Bus (USB) oscilloscopes (model Handyscope HS4-5,

TiePie engineering). Each oscilloscope can record up to four channels. Three oscilloscopes were connected and synchronized to allow electrical characterization of the nine-channel HVPS.

The current and power consumption data were estimated using a shunt resistor method (fig. S18A), where a 1-megohm resistor was connected in series with a TVMDE actuator. The voltages across the actuator and the resistor were simultaneously measured using two separate channels from the USB oscilloscope. The TVMDE actuator was charged for 500 ms and then discharged for 500 ms during each test at different actuation voltage, corresponding to an actuation cycle of 1 Hz. For each data point, the current was calculated by $I = \frac{V_R}{R}$, and the instantaneous power can be calculated by $P = I \times V_T$, where V_R is the voltage across the resistor and V_T is the voltage across the actuator.

Haptic perception test

The intensity, frequency, and pattern perception tests were performed on seven healthy volunteers (four female and three male individuals, with ages from 18 to 40). The average age of the volunteers is 29, with an SD of 7.5. During the test, the participants wore HAMS on their hands for haptic feedback and provided verbal response of the tactile sensation they received. HAMS was powered by the HVPS. All participants provided their consent before the test, and all experimental protocols for this human subject test were approved by the University of California, Los Angeles Institutional Review Board (UCLA IRB) (IRB #24-000170).

XR system

Oculus Quest 2 was selected for its high-resolution display (1080 × 1200) and integrated hand tracking. Virtual scenes were developed using Unity, and custom scripts were written in C# to enable dynamic interaction between the virtual hand and the environment. HAMS was connected to the HVPS, and the microcontroller on the HVPS received serial command from the PC and activated HAMS accordingly.

Actuator control in the XR demonstration scenes

In the rain scene, when rain was detected on hand, the actuators received the command to produce a set pattern at set intensity and frequency. The light rain command charged each actuator to a voltage of around 1800 V for 500 ms, while the heavy rain command charged each actuator to a voltage of around 2500 V for 120 ms.

In the ball scene, an invisible 3-by-3 grid was placed in the palm of the virtual hand. Each square within the grid corresponds to each actuator element in HAMS. When the ball rolled in the hand, it collided with exactly one square within the grid, and the corresponding actuator will then be charged to around 2800 V. Adjacent actuators were also programmed to actuate at lower voltages.

Actuator data during XR demonstrations

The voltages across the actuators in the rain scene and the ball scene were measured using the USB oscilloscope similar to what was mentioned in a previous section. To obtain the force data, a curve fitting was first performed to model the relationship between voltage and force data. The curve fitting used an exponential function and the force data as measured in Fig. 2B for 4-mm TVMDEs. Last force output was calculated from the measured voltage data using the fitted curve, and the force heatmaps were plotted.

Supplementary Materials

The PDF file includes:
Figs. S1 to S23
Table S1
Legends for movies S1 to S8

Other Supplementary Material for this manuscript includes the following:
Movies S1 to S8

REFERENCES AND NOTES

1. H. Bai, S. Li, R. F. Shepherd, Elastomeric haptic devices for virtual and augmented reality. *Adv. Funct. Mater.* **31**, 2009364 (2021).
2. K. R. Pyun, J. A. Rogers, S. H. Ko, Materials and devices for immersive virtual reality. *Nat. Rev. Mater.* **7**, 841–843 (2022).
3. B. C. M. Murray, B. N. Peele, P. Xu, J. Spjut, O. Shapira, D. Luebke, R. F. Shepherd, "A variable shape and variable stiffness controller for haptic virtual interactions" in *2018 IEEE International Conference on Soft Robotics (RoboSoft)* (IEEE, 2018).
4. M. Zhu, Z. Sun, Z. Zhang, Q. Shi, T. He, H. Liu, T. Chen, C. Lee, Haptic-feedback smart glove as a creative human-machine interface (HMI) for virtual/augmented reality applications. *Sci. Adv.* **6**, eaaz8693 (2020).
5. H. Son, H. Gil, S. Byeon, S.-Y. Kim, J. R. Kim, "RealWalk: Feeling ground surfaces While walking in virtual reality" in *Extended Abstracts of the 2018 CHI Conference on Human Factors in Computing Systems* (ACM, 2018).
6. X. Yu, Z. Xie, Y. Yu, J. Lee, A. Vazquez-Guardado, H. Luan, J. Ruban, X. Ning, A. Akhtar, D. Li, B. Ji, Y. Liu, R. Sun, J. Cao, Q. Huo, Y. Zhong, C. Lee, S. Kim, P. Gutruf, C. Zhang, Y. Xue, Q. Guo, A. Chempakasseril, P. Tian, W. Lu, J. Jeong, Y. Yu, J. Cornman, C. Tan, B. Kim, K. Lee, X. Feng, Y. Huang, J. A. Rogers, Skin-integrated wireless haptic interfaces for virtual and augmented reality. *Nature* **575**, 473–479 (2019).
7. Y. Huang, J. Zhou, P. Ke, X. Guo, C. K. Yiu, K. Yao, S. Cai, D. Li, Y. Zhou, J. Li, T. H. Wong, Y. Liu, L. Li, Y. Gao, X. Huang, H. Li, J. Li, B. Zhang, Z. Chen, H. Zheng, X. Yang, H. Gao, Z. Zhao, E. Song, H. Wu, Z. Wang, Z. Xie, K. Zhu, X. Yu, A skin-integrated multimodal haptic interface for immersive tactile feedback. *Nat. Electron.* **6**, 1–12 (2023).
8. Y. H. Jung, J.-Y. Yoo, A. Vázquez-Guardado, J.-H. Kim, J.-T. Kim, H. Luan, M. Park, J. Lim, H.-S. Shin, C.-J. Su, R. Schloen, J. Trueb, R. Avila, J.-K. Chang, D. S. Yang, Y. Park, H. Ryu, H.-J. Yoon, G. Lee, H. Jeong, J. U. Kim, A. Akhtar, J. Cornman, T. Kim, Y. Huang, J. A. Rogers, A wireless haptic interface for programmable patterns of touch across large areas of the skin. *Nat. Electron.* **5**, 374–385 (2022).
9. H. Jin, Y. Kim, W. Youm, Y. Min, S. Seo, C. Lim, C.-H. Hong, S. Kwon, G. Park, S. Park, H. J. Kim, Highly pixelated, untethered tactile interfaces for an ultra-flexible on-skin telehaptic system. *NPJ Flex Electron.* **6**, 82 (2022).
10. J.-H. Kim, A. Vázquez-Guardado, H. Luan, J.-T. Kim, D. S. Yang, H. Zhang, J.-K. Chang, S. Yoo, C. Park, Y. Wei, Z. Christiansen, S. Kim, R. Avila, J. U. Kim, Y. J. Lee, H.-S. Shin, M. Zhou, S. W. Jeon, J. M. Baek, Y. Lee, S. Y. Kim, J. Lim, M. Park, H. Jeong, S. M. Won, R. Chen, Y. Huang, Y. H. Jung, J.-Y. Yoo, J. A. Rogers, A wirelessly programmable, skin-integrated thermo-haptic stimulator system for virtual reality. *Proc. Natl. Acad. Sci. U.S.A.* **121**, e2404007121 (2024).
11. D. Li, J. Zhou, K. Yao, S. Liu, J. He, J. Su, Q. Qu, Y. Gao, Z. Song, C. Yiu, C. Sha, Z. Sun, B. Zhang, J. Li, L. Huang, C. Xu, T. H. Wong, X. Huang, J. Li, R. Ye, L. Wei, Z. Zhang, X. Guo, Y. Dai, Z. Xie, X. Yu, Touch IoT enabled by wireless self-sensing and haptic-reproducing electronic skin. *Sci. Adv.* **8**, eade2450 (2022).
12. Y. Wu, S. Zhang, Y. Yang, Z. Li, Y. Wei, Y. Ji, Locally controllable magnetic soft actuators with reprogrammable contraction-derived motions. *Sci. Adv.* **8**, eabo6021 (2022).
13. D. Kim, B. Kim, B. Shin, D. Shin, C.-K. Lee, J.-S. Chung, J. Seo, Y.-T. Kim, G. Sung, W. Seo, S. Kim, S. Hong, S. Hwang, S. Han, D. Kang, H.-S. Lee, J.-S. Koh, Actuating compact wearable augmented reality devices by multifunctional artificial muscle. *Nat. Commun.* **13**, 4155 (2022).
14. J. Barreiros, H. Claure, B. Peele, O. Shapira, J. Spjut, D. Luebke, M. Jung, R. Shepherd, Fluidic elastomer actuators for haptic interactions in virtual reality. *IEEE Robot. Autom. Lett.* **4**, 277–284 (2019).
15. X. Ji, X. Liu, V. Cacucciolo, Y. Civet, A. El Haitami, S. Cantin, Y. Perriard, H. Shea, Untethered feel-through haptics using 18-μm thick dielectric elastomer actuators. *Adv. Funct. Mater.* **31**, 2006639 (2021).
16. Y. Guo, Q. Qin, Z. Han, R. Plamthottam, M. Possinger, Q. Pei, Dielectric elastomer artificial muscle materials advancement and soft robotic applications. *SmartMat* **4**, e1203 (2023).
17. R. Pelrine, R. Kornbluh, Q. Pei, J. Joseph, High-speed electrically actuated elastomers with strain greater than 100%. *Science* **287**, 836–839 (2000).
18. A. Handler, D. D. Ginty, The mechanosensory neurons of touch and their mechanisms of activation. *Nat. Rev. Neurosci.* **22**, 521–537 (2021).
19. S. Biswas, Y. Visell, Haptic perception, mechanics, and material technologies for virtual reality. *Adv. Funct. Mater.* **31**, 2008186 (2021).

20. C. Keplinger, T. Li, R. Baumgartner, Z. Suo, S. Bauer, Harnessing snap-through instability in soft dielectrics to achieve giant voltage-triggered deformation. *Soft Matter* **8**, 285–288 (2012).

21. R. Vertechy, A. Frisoli, M. Bergamasco, F. Carpi, G. Frediani, D. De Rossi, Modeling and experimental validation of buckling dielectric elastomer actuators. *Smart Mater. Struct.* **21**, 094005 (2012).

22. I. Koo, K. Jung, J. Koo, J. Nam, Y. Lee, H. Choi, "Wearable fingertip tactile display" in *2006 SICE-ICASE International Joint Conference* (IEEE, 2006).

23. D.-Y. Lee, S. H. Jeong, A. J. Cohen, D. M. Vogt, M. Kollosche, G. Lansberry, Y. Mengüç, A. Israr, D. R. Clarke, R. J. Wood, A wearable textile-embedded dielectric elastomer actuator haptic display. *Soft Robot.* **9**, 1186–1197 (2022).

24. H. Phung, C. T. Nguyen, T. D. Nguyen, C. Lee, U. Kim, D. Lee, J. Nam, H. Moon, J. C. Koo, H. R. Choi, Tactile display with rigid coupling based on soft actuator. *Meccanica* **50**, 2825–2837 (2015).

25. E. Acome, S. K. Mitchell, T. G. Morrissey, M. B. Emmett, C. Benjamin, M. King, M. Radakovitz, C. Keplinger, Hydraulically amplified self-healing electrostatic actuators with muscle-like performance. *Science* **359**, 61–65 (2018).

26. G. Grasso, S. Rosset, H. Shea, Fully 3D-printed, stretchable, and conformable haptic interfaces. *Adv. Funct. Mater.* **33**, 2213821 (2023).

27. Y. Shi, E. Askounis, R. Plamthottam, T. Libby, Z. Peng, K. Youssef, J. Pu, R. Pelrine, Q. Pei, A processable, high-performance dielectric elastomer and multilayering process. *Science* **377**, 228–232 (2022).

28. G. Frediani, H. Boys, M. Ghilardi, S. Poslad, J. J. C. Busfield, F. Carpi, A soft touch: Wearable tactile display of softness made of electroactive elastomers. *Adv. Mater. Technol.* **6**, 2100016 (2021).

29. E. Leroy, R. Hinchet, H. Shea, Multimode hydraulically amplified electrostatic actuators for wearable haptics. *Adv. Mater.* **32**, 2002564 (2020).

30. A. K. Han, S. Ji, D. Wang, M. R. Cutkosky, Haptic surface display based on miniature dielectric fluid transducers. *IEEE Robot. Autom. Lett.* **5**, 4021–4027 (2020).

31. W. Yuan, L. B. Hu, Z. B. Yu, T. Lam, J. Biggs, S. M. Ha, D. J. Xi, B. Chen, M. K. Senesky, G. Grüner, Q. Pei, Fault-tolerant dielectric elastomer actuators using single-walled carbon nanotube electrodes. *Adv. Mater.* **20**, 621–625 (2008).

32. E. Hajiesmaili, D. R. Clarke, Dielectric elastomer actuators. *J. Appl. Phys.* **129**, 151102 (2021).

33. M. Gao, H. Wu, R. Plamthottam, Z. Xie, Y. Liu, J. Hu, S. Wu, L. Wu, X. He, Q. Pei, Skin temperature-triggered, debonding-on-demand sticker for a self-powered mechanosensitive communication system. *Matter* **4**, 1962–1974 (2021).

34. A. Minaminosono, H. Shigemune, T. Murakami, S. Maeda, Untethered rotational system with a stacked dielectric elastomer actuator. *Smart Mater. Struct.* **30**, 065007 (2021).

35. S. Schlatter, P. Illenberger, S. Rosset, Peta-pico-Voltron: An open-source high voltage power supply. *HardwareX* **4**, e00039 (2018).

36. S. K. Mitchell, T. Martin, C. Keplinger, A pocket-sized ten-channel high voltage power supply for soft electrostatic actuators. *Adv. Mater. Technol.* **7**, 2101469 (2022).

37. C. Hatzfeld, T. A. Kern, *Engineering Haptic Devices: A Beginner's Guide* (Springer, 2014).

38. X. Zhao, Z. Suo, Method to analyze programmable deformation of dielectric elastomer layers. *Appl. Phys. Lett.* **93**, 251902 (2008).

39. X. Zhao, W. Hong, Z. Suo, Electromechanical hysteresis and coexistent states in dielectric elastomers. *Phys. Rev. B* **76**, 134113 (2007).

40. Z. Suo, X. Zhao, W. Greene, A nonlinear field theory of deformable dielectrics. *J. Mech. Phys. Solids* **56**, 467–486 (2008).

41. X. Zhao, Z. Suo, Theory of dielectric elastomers capable of giant deformation of actuation. *Phys. Rev. Lett.* **104**, 178302 (2010).

42. N. Goulbourne, E. Mockensturm, M. Frecker, A nonlinear model for dielectric elastomer membranes. *J. Appl. Mech.* **72**, 899–906 (2005).